HIGH-RESOLUTION PIEZOPOLYMER ACOUSTIC BEARING ESTIMATOR

Shawn E. Burke
The Center for Photonics Research, and
Department of Aerospace and Mechanical Engineering
Boston University
Boston, Massachusetts 02215
burke@bu.edu

Joseph A. Paradiso
MIT Media Laboratory
Cambridge, Massachusetts 02139
joep@media.mit.edu

to be presented at

Second Technical Conference on
Telecommunications R&D in Massachusetts
12 March 1996
University of Massachusetts, Lowell

High-resolution piezopolymer acoustic bearing estimator

Shawn E. Burke
The Center for Photonics Research
Boston University
Boston, Massachusetts 02215

Joseph A. Paradiso
MIT Media Laboratory
Cambridge, Massachusetts 02139

Abstract
A novel acoustic sensor is described that utilizes two coincident, distributed, shaded PVDF piezopolymer sensors to provide high-resolution acoustic source bearing estimates. Sensor shading is accomplished by shaping the charge collection electrodes deposited on the sensing layer. When these two sensor shadings are matched via a derivative in space, the ratio of their signal outputs is linearly proportional to the direction cosine of an incident acoustic field; this is an extension of the well-known "monopulse" concept in radar. By using derivative-matched aperture shadings, the monopulse ratio is independent of frequency. This, combined with PVDF's flat frequency response, facilitates wide bandwidth application of the sensor. A hardware realization of the sensor concept is described, and experimental results are presented for an underwater (e.g., sonar) implementation of the sensor. Agreement between theory and experiment for bearing estimation is excellent for source locations within the sum aperture's main lobe. For SNR greater than 20dB, the ratio of the sum aperture's 3dB main lobe width to the bearing estimation standard deviation (the "split ratio") approaches 100. The sensor described here provides a means of obtaining high spatial resolution acoustic bearing estimates for applications such as source tracking for teleconferencing, novel audio/user interfaces, and multimedia applications.

Keywords: Monopulse sensor, acoustic bearing estimator; multimedia sensor.

1. Introduction

Conventionally, acoustic sensing systems achieve acoustic direction finding by comparing the output of two or more discrete transducers with identical spatial response characteristics separated by a known, fixed spacing. This physical separation provides a spatial phase shift between the transducers, which facilitates direction estimation from time delay measurements of by electronic steering. The performance of these devices is limited in resolution by aperture length, side lobes, etc. The arrays can be bulky and complex, and necessitate substantial signal processing hardware and software.

Monopulse sensing achieves acoustic direction finding by comparing the output of two receivers which have known but non-identical spatial response characteristics. Monopulse processing is typically based upon the comparison of sum and difference beam patterns from pairs of discrete sensors [1,2]. In the present application, directional response is determined by the specific choice of transducer aperture shadings, e.g., spatial gain weightings, for two coincident, distributed sensors, in a technique called "wideband

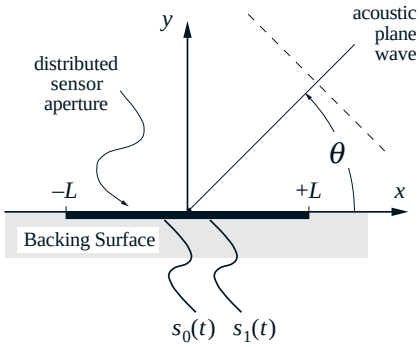

Fig. 1: Oblique incidence geometry

monopulse" [3]. The outputs from two such receivers are related by a scale factor that is a function of the acoustic field's incidence angle θ (Fig. 1), the direction of sonar echoes returning from an object of interest.

If the second aperture shading function is constrained to equal the spatial derivative of the first along the *x*–axis, then the two sensor outputs at every instant in time are linearly related, with the proportionality constant equal to the cosine of the pressure field's incidence angle defined in Fig. 1. Derivative-matching provides the requisite spatial phase difference between the sensor apertures to facilitate direction finding. The computation of the incidence angle (e.g., direction) follows directly; direction finding is accomplished without steering. An example of derivative-matched shadings appears in Fig. 2; there are many other possible derivative-matched aperture shadings. Note that the derivative-matching constraint itself does not necessitate that an aperture have a particular symmetry. Rather, if the first aperture is even-symmetric, the second, derivative-matched aperture will be odd-symmetric, and vice versa.

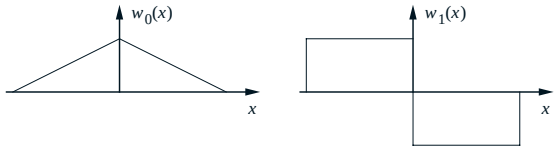

Fig. 2: Example derivative-matched aperture shading functions.

These spatially-continuous shadings can only be implemented in practice using spatially-distributed sensing. The implementation considered here uses the piezopolymer film polyvinylidene fluoride (often referred to as PVF_2, or PVDF – the piezoelectrically active form of Kynar) to implement the spatially-distributed sensors. By spatially-weighting the collection of charge on these sensors, so that the distributed transducer's aggregate output is proportional to a spatially-weighted integral of the applied normal stress, one can implement the shadings shown above exactly in 2-D.

The use of distributed sensing technology offers many advantages over a large number of discrete sensing elements, such as elimination of directional ambiguities and bandwidth constraints associated with discrete sensor implementations of wideband monopulse [3], reduced number of signal channels, reduced complexity and weight, etc. The wideband monopulse technique, coupled with the light-weight transducer implementation described

in the sequel, is therefore an attractive solution for space-constrained application environments.

In the following sections, the wideband monopulse processing concept is briefly summarized. Then, a means for realizing derivative-matched sensor shadings using distributed piezoelectric polymer film is described. An experimental application of the concept to sonar bearing estimation is presented, and data from a series of in-water tests is summarized. Applications of the wideband monopulse sensor germane to teleconferencing and multimedia are proposed, and directions for future work are summarized.

2. The Wideband Monopulse Concept

The general problem of monopulse bearing estimation using aperture shading as the major design parameter will now be examined; the derivation complements that presented in [3,4,5. Consider a monochromatic acoustic plane wave in a homogeneous, isotropic, non-dispersive medium, whose wave vector **k** is directed at an angle θ with respect to the (x,y) coordinate system shown in Fig. 1. The wave is traveling right-to-left. We shall consider a sensor aperture, or apertures, deposited along $x \in [-L, L]$ along the surface $y = 0$. The pressure field in the acoustic medium is described mathematically as

$$p(\mathbf{x},t) = Pe^{i(kx\cos\theta + ky\sin\theta\omega t)} \ . \tag{1}$$

Any two sensors having shadings $w_0(x)$ and $w_1(x)$ over $x \in [-L, L]$ will have outputs $s_0(t)$ and $s_1(t)$, respectively, along the sensor's surface $y = 0$ of the form

$$s_0(t) = \int_{-L}^{+L} w_0(x) P e^{ikx\cos\theta + \omega t} dx \ , \tag{2}$$

$$s_1(t) = \int_{-L}^{+L} w_1(x) P e^{ikx\cos\theta + \omega t} dx \ . \tag{3}$$

We desire the ratio of the two signal outputs $s_0(t)$ and $s_1(t)$ to be linearly proportional to the cosine of the incidence angle θ for all time t: the wideband monopulse result. That is,

$$\frac{s_1(t)}{s_0(t)} = a\cos\theta \ , \tag{4}$$

where a is a frequency- and bearing-independent constant. This implies

$$\int_{-L}^{+L} w_1(x) e^{i(kx\cos\theta)} dx = -ik\cos\theta \int_{-L}^{+L} w_0(x) e^{i(kx\cos\theta)} dx \ . \tag{5}$$

Equation (5) provides a constraint on how the aperture shadings may be chosen to satisfy the wideband monopulse relation (4). In particular, if

$$w_1(x) = \frac{d\left[w_0(x)\right]}{dx} \ , \tag{6}$$

e.g., if the second sensor shading is the spatial derivative of the first, then equation (5) is satisfied.

Upon defining the trace number $\tilde{k}$ as $\tilde{k} \equiv k\cos\theta$, one then sees that

$$s_0(t) = w_0\left(\tilde{k}\right)\exp(i\omega t) \ , \tag{7}$$

where $w_0\left(\tilde{k}\right)$ is the wavenumber transform of the shading function $w_0(x)$ with respect to the trace wavenumber; note that $w_0(x) = w_1(x) = 0$ for $|x| > L$. Similarly,

$$s_1(t) = w_1\left(\tilde{k}\right)\exp(i\omega t) \ . \tag{8}$$

Using the derivative-matching criteria (6), and the differentiation theorem of Fourier transforms, one notes

$$s_1(t) = i\tilde{k}w_0\left(\tilde{k}\right)\exp(i\omega t) \ ; \tag{9}$$

as anticipated, the ratio of the signal outputs (9) and (8) is linearly proportional to the direction cosine.

As an example of derivative-matched apertures, consider the derivative-matched shadings depicted in Fig. 2. The shadings w_0 and w_1 are described mathematically as

$$w_0(x,L) = \langle x+L\rangle^1 - 2\langle x\rangle^1 + \langle x-L\rangle^1 \tag{10}$$

and

$$w_1(x,L) = \langle x+L\rangle^0 - 2\langle x\rangle^0 + \langle x-L\rangle^0 \ . \tag{11}$$

The MacCauley notation $\langle x-a\rangle^0$ and $\langle x-a\rangle^1$ denotes step and ramp functions, respectively, "turning on" at $x = a$. In the present application one notes that the shading $w_0(x)$ cannot have MacCauley components of exponent less than 1, or the derivative-matched shading will require delta functions, which cannot be realized using distributed piezoelectric transducers. For finite apertures, this requires w_0 to vanish at the endpoints $x = \pm L$.

The trace wavenumber transforms of the shading functions are

$$w_0\left(\tilde{k},L\right) = \frac{-e^{-i\tilde{k}L}\left(e^{i\tilde{k}L}-1\right)^2}{\tilde{k}^2 L} \tag{12}$$

and

$$w_1\left(\tilde{k}, L\right) = -i\tilde{k} w_0\left(\tilde{k}, L\right) , \tag{13}$$

respectively; equation (13) exploits the differentiation theorem of Fourier transforms. These transforms are, of course, proportional to the aperture beam patterns. Since the shading (10) is even-symmetric, the shading transform $w_0\left(\tilde{k}\right)$ is real, and possesses a broadside maximum (main lobe). The derivative-matched shading (11), which is odd-symmetric, has an imaginary shading transform $w_1\left(\tilde{k}\right)$ which possesses a broadside null; note that, with respect to $w_0(x)$, the matched shading $w_1(x)$ is a spatial differentiator. The shadings depicted in Fig. 2 provide the best SNR either (1) near broadside, or (2) at frequencies wherein the target lies within the main lobe of the shading $w_0(x)$.

3. Sensor Design and Evaluation

Hardware and Electronics Concept

One might choose to approximate the derivative-matched shadings using discrete sensors; discrete element arrays are widely available. However, this only provides an approximation of distributed shadings. (One might consider a shading w_0 consisting of an array of delta functions, representing an array of point hydrophones. However, the corresponding derivative-matched shading would then consist of discrete pressure gradient hydrophones.) One would have to ensure that the sensor elements are half-wavelength spaced or closer to avoid spatial aliasing; this imposes an implicit frequency limit. Even then, the error introduced in using a discrete approximation of distributed shadings leads to a proportionality between the s_0 and s_1 signal outputs that, even with an integration, is frequency dependent [3]; the wideband character of this monopulse concept is lost. Consequently, one is led to investigate the utility of distributed sensors.

A prototype distributed sensor stave design and fabrication was undertaken to (1) demonstrate a simple, rugged monopulse sensor design approach; (2) validate the concept of shading a distributed sensor via charge collection electrode shaping; and (3) demonstrate target bearing estimation using the monopulse processing scheme, and assess the sensor's resolution.

The sensor stave concept is shown in Fig. 3 [6,7,8]. The sensing material is a 110 micron layer of Amp uniaxially-poled polyvinylidene fluoride (PVDF). PVDF is a polymer that can be polarized, or made piezoelectrically active, by appropriate processing during manufacture. In its polarized form PVDF is essentially a tough, flexible piezoelectric crystal. It is commercially available as a thin polymeric film, and is used in many sonar sensing applications [9]. When subjected to an applied normal stress (e.g., an acoustic field) a voltage or electric field potential develops across its faces. This response occurs locally over the entire area of the film in proportion to the local applied stress, making it a distributed parameter sensor. The signal output is the integrated sum of these voltages distributed over the area of the charge collection electrodes.

The derivative-matched shading requirement (7) developed in the previous section essentially requires two distributed, shaded sensors to be simultaneously implemented over the same aperture. In the present application, the charge collection electrodes are shaped so as to realize the necessary shading functions using the PVDF film. This

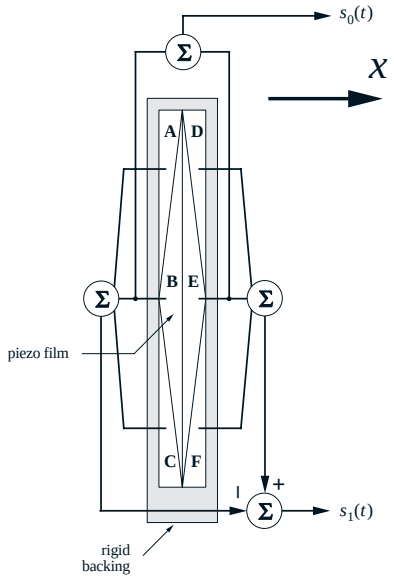

Fig. 3: PVDF monopulse sensor stave concept.

technique is an extension of active structural vibration control transducer design methods, as well as a real-time hydrodynamic center-of-pressure sensor concept [10,11]. Consider the charge collection electrode pattern shown in Fig. 3. An acoustic plane wave impinges on the sensor, where the wavevector lies in the *x*-*y* plane. The area subtended by electrode B increases linearly with x until it reaches a maximum at the centerline. The area subtended by electrode E decreases linearly with x, having zero width at $x = +L$ (the right edge of the sensor's active area in the Figure). Since the electrodes define the area over which the charge produced by the PVDF film is collected, and since the spanwise phase variation of the acoustic field is zero (the wavevector was assumed to lie in the *x*-*y* plane), the electrodes B and E provide a spatial weighting of the sensed acoustic field corresponding to the shading $w_0(x)$ along the x-axis, as realized by the signal s_0 depicted in Fig. 3.

Similarly, when the signal outputs from electrodes A, B, and C are summed, this corresponds to a uniform weighting of the sensed acoustic field over $-L \le x \le 0$. When the signal outputs from electrodes D, E, and F are summed, this corresponds to a uniform weighting of the sensed acoustic field over $0 \le x \le +L$. The difference of these two signals, represented by the signal $s_1(t)$, corresponds to the split-aperture shading $w_1(x)$ along the x-axis. Interestingly enough, the electrode pattern shown in Fig. 3 allows one to realize two shaded distributed transducers simultaneously over the same aperture using a single PVDF sensing layer. This obviates the need for using two laminated PVDF sensing layers, each of which would embody the shadings $w_0(x)$ and $w_1(x)$ separately.

In the sensor shown in Fig. 3, the piezopolymer sensing film is bonded to a 1.01" thick backing layer of G-10 circuit board material. G-10 was chosen because of its high stiffness-to-weight ratio, as compared to steel or brass. This 1.01" thick backer consists of a 10-mil layer of copper-plated circuit board laminate, fused to a 1" thick G-10 layer. The 10-mil laminate is etched with the desired charge collection electrode pattern, including solder tabs. Etching the backer has proven superior to etching the charge

collection electrodes directly on pre-plated film, as the circuit board tends to not "swim" and lead to registration problems. The unplated face of the sensing film is then bonded to the etched electrodes with a high-permittivity epoxy, suitably deaerated. A uniformly plated outer conductor provides a common electrode. Leads are adhered, and then fed through the backer to circuitry mounted directly on the back of the stave in an integral enclosure. Signals from each subaperture run topside to analog signal conditioning circuitry, including summers, through water-tight cables and connectors.

For the ensuing underwater tests and calibrations, the entire sensor stave is potted in a deaerated PRC-1570 polyurethane layer; this encapsulation would not be necessary for in-air applications. The encapsulant is cured at a lower-than-normal temperature of 90˚ C so as to avoid depoling the piezopolymer film – PVDF has a Curie point of approximately 100˚ C. This lengthens the polyurethane cure time significantly, but seems to have no adverse acoustical side-effects.

Front-end amplifiers buffer each of the 6 subaperture outputs. These consists of a non-inverting gain stage designed around a low voltage-noise AD745 JFET operational amplifier, ($3nV/\sqrt{Hz}$) followed by a unity-gain differential line driver that sends the subaperture signal across a shielded 600 Ω pair to an external electronics module. The gain stage was designed to have a high-pass response in order to attenuate low-frequency background from mechanical disturbances and PVDF thermal response; it provides a gain of 27 dB for frequencies above 200 *Hz*, rolling off to unity at DC. The front-end was realized on two small 3-channel circuit cards, mounted in a small compartment directly behind the sensor stave. In order to improve shielding, a copper ground plane is laminated behind the subaperture electrodes. The common (outside) plated electrode of the PVDF is floated slightly from ground to allow a signal to be capacitively coupled into all subaperture electrodes for test and calibration purposes.

In the external electronics module, the outputs from the front-end are differentially received, further amplified, then rolled off by a bank of second-order high-pass filters with cutoff at 3 *kHz*, again to attenuate mechanical noise and generic background (before filtering, these signals are summed, then provided to an audio tap for diagnostic monitoring and to an adjustable discriminator for self-triggering). The 6 filter outputs are then appropriately summed and differenced to form numerator (s_1) and denominator (s_0) signals. Unwanted background is attenuated by adjusting a tracking pair of parametric high-pass filters (based around a 4'th-order CEM 3320 VCF) and selecting an appropriate low-pass rolloff. The filtered numerator (N) and denominator (D) signals are then digitized and stored by a Macintosh-based data acquisition system. After correcting for the 90° phase difference with an all-pass filter, these outputs are also directed to a circuit that latches the N and D signals at the peak D value over a gated interval (to minimize the scale errors from noise), then takes the analog ratio (N/D) to provide a coarse bearing indicator that is useful during system setup and adjustment.

The electronics were designed to provide maximum flexibility during prototype testing. Production designs can be much simpler; i.e. the front-end plus sum and differencing can be realized with microchips mounted directly on the edges of the sensor stave, occupying minimal volume. The resulting pair of N and D signals can be digitized directly with minimal filtering, allowing further signal processing and analysis to be realized entirely in software. The addition of a time-varying gain (TVG) stage would also maximize the dynamic range of the digitized signal.

3. Sensor Characterization

The monopulse sensors and associated signal conditioning electronics were calibrated in a salt water test tank. Two sensors were tested: one with a 20˚ sum aperture main lobe, and one with a 30˚ sum aperture main lobe. The sound source was an ITC 1042 omnidirectional ceramic transducer, driven using a Techron 200*W* power supply. The source and monopulse receive sensor were suspended in mid water column by aluminum fixtures. The sensor was mounted with its bearing resolution ("z") axis lying in the horizontal plane, facing the source. By fixing the location of the receive sensor, the bearing to the source was varied by translating the projector across the width of the tank in fixed increments. The dimensions of the tank allowed both the 20˚ and 30˚ coverage sensors to be calibrated over their entire sum aperture main lobe. Additional test parameters are listed in Table 1.

Tests were conducted by driving the projector with a 100*kHz* CW pulse, sourced by an Ithaco signal generator, and gated using custom triggering/timing electronics. The signal outputs of the monopulse sensor under test were fed to a custom buffer/summing amplifier unit, low-pass filtered, and digitized using a Mac II-based DAS built around a National Instruments A2000 A/D converter board and LabVIEW software. Signals were sampled at 500 *kHz*, and saved to disk files for later analysis. Twenty samples were recorded for each fixed projector location. The time records were of sufficient length to include the entire received CW gate. Tests were conducted for both the 20˚ and 30˚ sensors.

Table 1: Test Parameters

Test tank length	12’
Test tank width	6’
Water depth	4.5'
Projector depth	27"
Sensor depth	27" (to sensor centroid)
Trigger delay	1.4 *msec*
LPF	100 *kHz* (corner freq.)
HPF	2*kHz* (corner freq.)
Signal type	gated 100*kHz* CW pulse
Gate width	66 *msec*

The data files generated during the calibration tests were stored in a Lab-VIEW-native format. These were translated to MATLAB binary format using a custom LabVIEW vi. Data reduction was undertaken in MATLAB using Hilbert transform-based techniques [12]. This yielded a series of scaled direction cosine estimates for each fixed projector location, for each sensor. These data were scaled, and compared to the ideal theoretical $cos(\theta)$ monopulse proportionality.

The results are plotted in Figures 4 and 5 for the 20˚ and 30˚ sensors, respectively. The agreement between theory and experiment is excellent for the 20˚ sensor, demonstrating that it is behaving as a monopulse device. There is a minor systematic error in locating broadside, attributable to the test fixturing, that leads to the slight asymmetry about 0˚. The agreement between theory and experiment for the 30˚ sensor is also excellent. In addition to the minor systematic error, there is a small divergence from theory as one approaches the limits of the 30˚ coverage sector. This is attributable to the confines of

the test tank: for these data points the projector was nearly abutting the walls of the test tank. Nonetheless, the calibration also demonstrates that the 30˚ sensor was correctly behaving as a monopulse sensor.

Figures 4 and 5 demonstrate that the sensor does indeed function as a monopulse sensor. Equally as important is the sensor's bearing resolution capability. Since it does not function as a beamformer, one cannot characterize localization performance in terms of, say, 3dB beamwidth or directivity index (DI). One uses instead a statistical characterization of bearing resolution, based up the standard deviation of the bearing estimate in the presence of a spatially isotropic acoustical noise field and preamp noise. Such a model has been developed in [13], where it is shown that the standard deviation of the bearing estimate in radians is

$$\sigma_{\hat{u}} = \left(\frac{.8\lambda}{2\pi L}\right)\sqrt{\frac{2+\gamma_n+\gamma_s}{SNR}}\ , \tag{14}$$

where L is the sensor aperture length in the monopulse direction, γ_n is a parameter that equals 0 for isotropic noise, and equals .55 for preamp noise, γ_s is a parameter that characterizes the extent of the source compared to the beamwidth in the monopulse direction, and SNR is the signal to noise ratio. Note that the standard deviation of the bearing estimate goes inversely as the square root of the signal to noise ratio.

To normalize the results for various coverage sector sizes, one typically computes the *split ratio,* defined as the ratio of the 3dB beamwidth in the monopulse direction to the standard deviation of the bearing estimate, vis

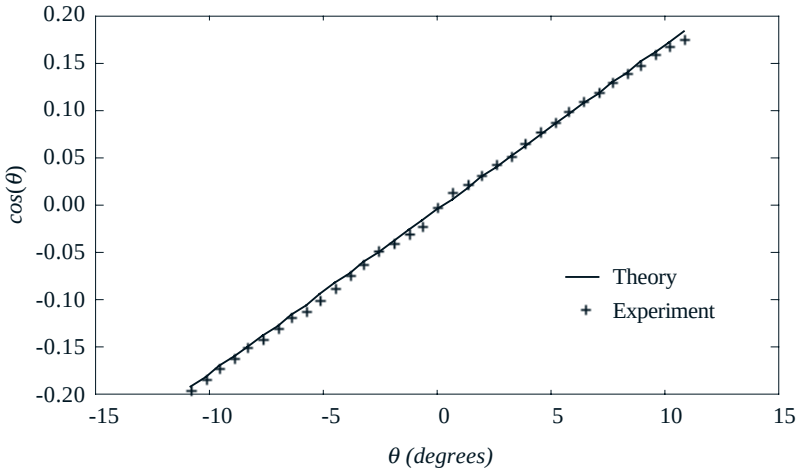

Figure 4: 20˚ sector bathymetric sensor calibration.

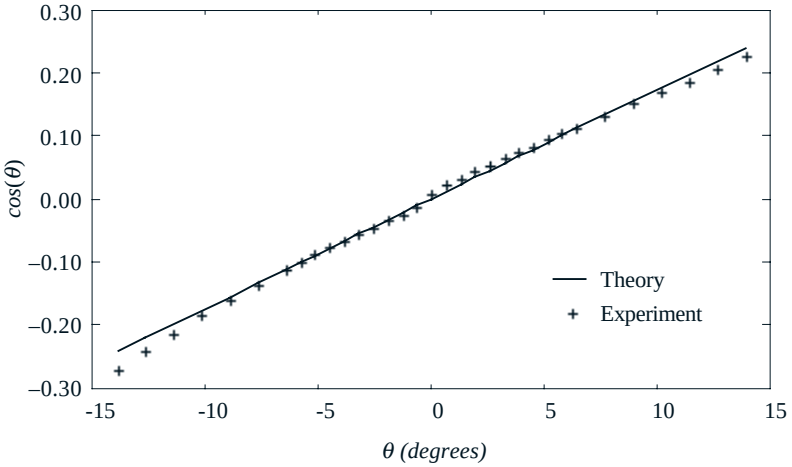

Figure 5: 30˚ sector bathymetric sensor calibration.

$$split\ ratio \equiv \frac{\theta_{3dB}}{\sigma_{\hat{u}}}\ ; \tag{15}$$

The split ratio is a measure of the bearing resolution improvement monopulse sensing provides as compared to using the sum aperture main lobe alone to spatially resolve a target. The split ratio is plotted in Figure 6 for our monopulse sensors operating at the 100kHz sonar frequency. One notes that, for a 20dB SNR (sum channel), monopulse estimation will resolve targets ~11 times finer than a beamformer of equal aperture.

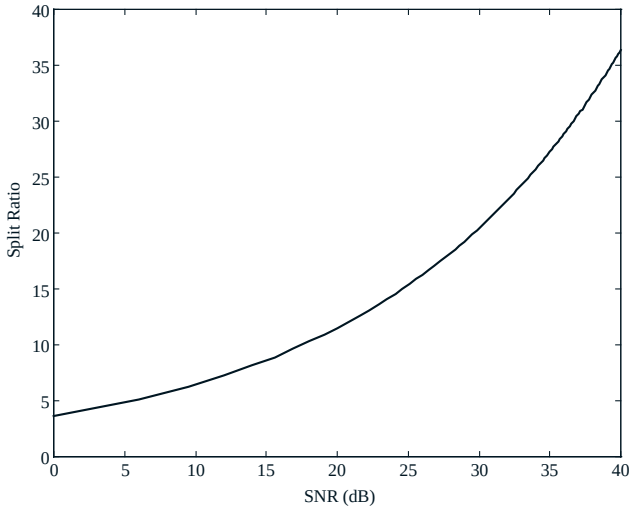

Figure 6: Split ratio estimate; includes preamp noise and isotropic acoustic background.

4. Applications and Future Direction

Although the results of the previous section demonstrated the efficacy of the acoustic bearing sensor in water, the principle of operation should work equally as well in air. Because of their simple readout and frequency-independent operation, there are many applications for such devices as new user interface sensors. The most exciting are in the passive listening mode. For instance, these sensors can determine the azimuthal bearing of sonic events (i.e., finger snapping, voice) generated by individuals in virtual environments [14] to enhance computer interaction; such a coverage concept is illustrated in Fig. 7. Intelligent cameras can react to sounds by not merely activating, but now by turning to point at the sound's origin. Future video and "movie" productions will employ additional information gathered in a shoot from other sensor channels (such as acoustic bearing information) in order to readily enable computer enhancement and intelligent editing [15]. The inexpensive nature of such PVDF sensors enable their application in may "smart" objects that will soon be introduced as computing and communication drop in price and become liberally embedded throughout our environment [16]. This sensor also provides advantages for active in-air sonar, i.e., a simple bearing measurement can be performed for multiple sonar transponders (on objects in a room or performers on a set) operating at different frequencies, permitting easy disambiguation.

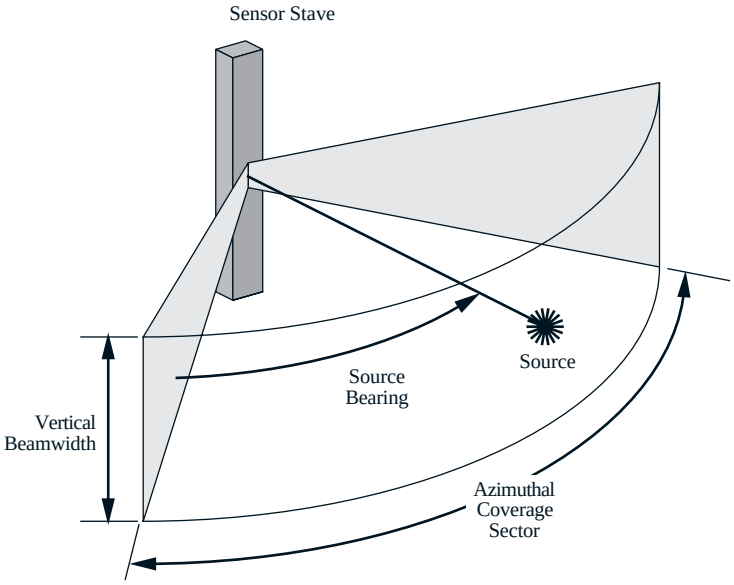

Figure 7: Coverage Concept.

Devices for in-air use are now under construction. In order to operate efficiently for passive listening at the lower frequencies of human hearing vs. the sonar frequencies of the aforestated investigations, non-hydrostatic mode PVDF sensors are being designed.

References

[1] D.R. Rhodes, *Introduction to Monopulse*, New York: McGraw-Hill Book Company (1959).

[2] S.M. Sherman, *Monopulse Principles and Techniques*, Dedham MA: Artech House (1984).
[3] T.L. Henderson, "Matched beam theory for unambiguous broadband direction finder", *Journal of the Acoustical Society of America*, **78**(2), pp. 563-573 (1985).
[4] S.G. Lacker and T.L. Henderson, "Wideband monopulse sonar performance: Cylindrical target simulation using an acoustic scattering center model", *IEEE Journal of Oceanic Engineering*, **15**(1), pp. 32-41 (1990).
[5] T.L. Henderson, "Wideband monopulse sonar: Processor performance in the remote profiling application", *IEEE Journal of Oceanic Engineering*, **OE-12**(1), pp. 182-197 (1987).
[6] S. Burke and J. Hubbard, "Wideband, derivative-matched, continuous aperture acoustic transducer", United States Patent No. 5,237,542 (17 August 1993).
[7] S. Burke and J. Hubbard, "Wideband, derivative-matched, continuous aperture acoustic transducer", United States Patent 5,327,397 (5 July 1994).
[8] S. Burke, "Curvilinear, wideband, projected derivative-matched, continuous aperture acoustic transducer", United States Patent 5,373,483 (13 December 1994).
[9] W.J. Hughes, "Advanced underwater sensors using piezoelectric materials", *Sea Technology*, pp. 43-45, (August 1990).
[10] S.E. Burke and J.E. Hubbard, Jr., "Active vibration control of a simply supported beam using a spatially distributed actuator", *IEEE Control Systems Magazine*, pp. 25-30 (August 1987).
[11] J.E. Hubbard, Jr., and S.E. Burke, "Pressure distribution characterization system", United States Patent No. 5,054,323 (8 October 1991).
[12] S. Burke, "Hilbert transforms: Application to wideband monopulse data reduction", Draper Laboratory Technical Memorandum ESC-92-173 (May 1992).
[13] K. Houston, “Performance analysis for a wideband monopulse side-scan sonar”, Draper Laboratory Technical Memorandum ETB-93-166, (May 1993).
[14] P. Maes *et al*, “The ALIVE system: Full-body interaction with autonomous agents”, *Proceedings of Computer Animation ‘95*, IEEE Press (1995).
[15] V. Bove, Jr., “Object-oriented Television”, *SMPTE Journal*, **104**, pp. 807-807 (1995).
[16] J. Paradiso, “The interactive balloon: Sensing, actuation, and behavior in a common object”, submitted to the *IBM Systems Journal* (1996).